Research in Astronomy and Astrophysics, 23:065013 (10pp), 2023 June https://doi.org/10.1088/1674-4527/accbb3

Extraction and Analysis of Coronal High-temperature Components Based on Outlier Detection

Li-Yan Sun[1,2], Kai-Fan Ji[1], Jun-Chao Hong[1], and Hui Liu[1]
[1] Yunnan Observatories, Chinese Academy of Sciences, Kunming 650216, China; sunliyan@ynao.ac.cn, liuhui@ynao.ac.cn
[2] University of Chinese Academy of Sciences, Beijing 101408, China
Received 2023 February 20; revised 2023 March 24; accepted 2023 April 3; published 2023 May 23

Abstract

The extraction of high-temperature regions in active regions (ARs) is an important means to help understand the mechanism of coronal heating. The important observational means of high-temperature radiation in ARs is the main emission line of Fe XVIII in the 94 Å of the Atmospheric Imaging Assembly. However, the diagnostic algorithms for Fe XVIII, including the differential emission measure (DEM) and linear diagnostics proposed by Del based on the DEM, have been greatly limited for a long time, and the results obtained are different from the predictions. In this paper, we use the outlier detection method to establish the nonlinear correlation between 94 Å and 171, 193, 211 Å based on the former researches by others. A neural network based on 171, 193, 211 Å is constructed to replace the low-temperature emission lines in the ARs of 94 Å. The predicted results are regarded as the low-temperature components of 94 Å, and then the predicted results are subtracted from 94 Å to obtain the outlier component of 94 Å, or Fe XVIII. Then, the outlier components obtained by neural network are compared with the Fe XVIII obtained by DEM and Del's method, and a high similarity is found, which proves the reliability of neural network to obtain the high-temperature components of ARs, but there are still many differences. In order to analyze the differences between the Fe XVIII obtained by the three methods, we subtract the Fe XVIII obtained by the DEM and Del's method from the Fe XVIII obtained by the neural network to obtain the residual value, and compare it with the results of Fe XIV in the temperature range of 6.1–6.45 MK. It is found that there is a great similarity, which also shows that the Fe XVIII obtained by DEM and Del's method still has a large low-temperature component dominated by Fe XIV, and the Fe XVIII obtained by neural network is relatively pure.

Key words: Sun: corona – Sun: activity – methods: statistical – methods: data analysis – techniques: image processing

1. Introduction

The temperature of the solar corona is so high that it can be up to millions of kelvins, and the highest regions are often found in the core of the active regions (ARs), which even can reach 3 MK or higher. Understanding the physical mechanism of high-temperature regions is key to understanding the coronal heating mechanism, and one of its prerequisites is to achieve the localization of the high-temperature regions.

Most of the observations about the ARs began at Skylab (Orrall 1981) in the 1970s, but many researches have been found from the later space missions such as SMM (Hundhausen 1993), Yohkoh (Acton et al. 1992), SOHO (Domingo et al. 1995), TRACE (Golub et al. 1999), Hinode (Tsuneta et al. 2008), and Solar Dynamics Observatory (SDO) (Pesnell et al. 2012). The Atmospheric Imaging Assembly (AIA) (Lemen et al. 2012) on the SDO since its launch in 2010 has been producing high-resolution, high-quality images of the Sun's full solar corona in a 12 s cadence, with six of its seven extreme ultraviolet (EUV) channels dominated by iron emission lines: 94 Å (Fe XVIII), 131 Å (Fe VIII, Fe XX, Fe XXIII), 171 Å (Fe IX), 193 Å (Fe XII, Fe XXV), 211 Å (Fe XIV), 335 Å (Fe XVI). The 304 Å (He II) is mainly dominated by He emission lines.

The high temperature in the ARs leads to the emission typically observed in spectral EUV lines such as Fe XVI, Fe XVII, and Fe XVIII one of the main emission lines of 94 Å (Mulay et al. 2018). For this reason that the 94 Å and Fe XVIII are important features for locating the high-temperature regions.

Under the assumption that the plasma in the solar corona is optically thin and ionization equilibrium, the observed coronal intensity of a spectral channel can be expressed as:

$$I_{\rm ob} = A(z) \int_{T_{\rm e}} G(T_{\rm e}, N_{\rm e}) \varphi(T_{\rm e}) dT_{\rm e}. \quad (1)$$

Here $A(z)$ is the elemental abundance, $T_{\rm e}$ is the temperature of the electron and $N_{\rm e}$ is the number density of the electron. The contribution function, $G(T_{\rm e}, N_{\rm e})$, contains the relevant atomic parameters for each line and can be obtained using equilibrium ionization balance calculations. $\varphi(T_{\rm e})$ is considered

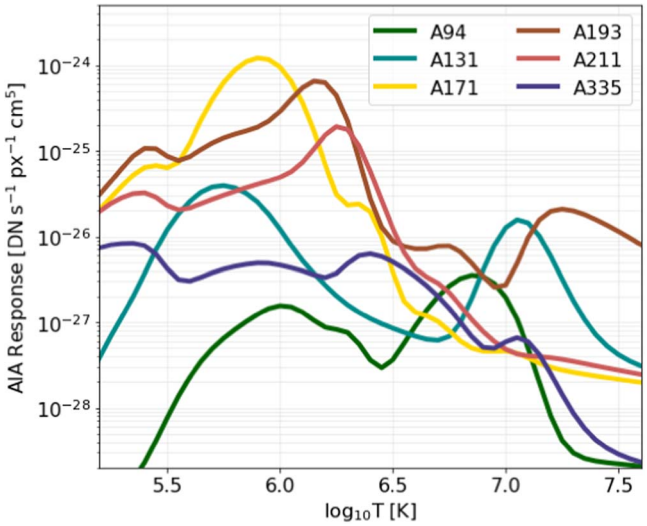

Figure 1. The response functions $\log_{10} T$ [K] for the 94, 131, 171, 193, 211, and 335 Å EUV channels of SDO/AIA.

differential emission measure (DEM), where h is the line-of-sight coordinate

$$\varphi(T_e) = N_e{}^2 \frac{dh}{dT_e}. \quad (2)$$

With the help of the DEM and the response functions computed using CHIANTI 7.0 (Landi et al. 2011) (see Figure 1), we can get the temperature of AIA different channels and their emission lines. O'dwyer et al. (2010) measured the DEMs of the coronal hole (CH), quiet Sun (QS), ARs, and flare plasma (FL) in the different AIA channels and predicted the count rates of AIA. From Table 1, it can be seen that the most important contribution of both the flare plasma and ARs comes from Fe XVIII (6.85 MK) in the 94 Å, while the ARs also contain Fe X and continuum. The QS and the CH are more complicated, and their main contribution comes from Fe X. Meanwhile, we can also find the ARs of the 94 Å only contain Fe XVIII, Fe X, and part of the continuum. The count rate of Fe XVIII is as high as 74%, which plus the count rates of the continuum can reach 91%. Accordingly, the Fe XVIII in the ARs of 94 Å that covers 6.45–7.0 MK can be considered as the high-temperature regions in the solar corona.

From Figure 2, it can be seen that the response functions of the 94 Å has a clear interval around 6.45 MK and is divided into two parts. The later part (from 6.45 to 7.0 MK) is dominated by Fe XVIII, the part from 5.5 to 6.0 MK mainly includes Fe VIII, Fe X; and the former part from 6.1 to 6.45 MK mainly includes Fe XIV, Fe XII. Therefore, we can extract the Fe XVIII by removing the low-temperature emission lines of the 94 Å.

Based on the DEM, Warren et al. (2012) used the 171 and the 193 Å to fit the high-temperature of 94 Å

$$I_{94\mathrm{warm}} = 0.39 \sum_{i=1}^{4} a_i \left[\frac{f I_{171} + (1-f) I_{193}}{116.54} \right]^i \quad (3)$$

where f obtained the best fit with $f = 0.31$ in the validation.

In 2013, Del Zanna (2013) fitted the Fe XVIII by combining the 171 Å and the 211 Å

$$I(\mathrm{Fe\ XVIII}) = I(94\ \text{Å}) - I(211\ \text{Å})/120 - I(171\ \text{Å})/450 \quad (4)$$

where the 211 Å is used to replace Fe XIV (Fe XIV occupies nearly half of the count rates in the ARs of 211 Å) and some of the cooler emission lines. The 171 Å is used to replace the weaker contributions such as Fe X, Fe VIII, and Fe IX. In addition, it can be seen that the 94 Å is fitted by the combination of 211 and 171 Å. Fe XVIII is 94 Å minus the combination. We make the combination of 211 and 171 Å is the low-temperature of 94 Å (94 Å(Del)).

Both two algorithms achieve a good agreement with the high-temperature component results computed by the DEM. Besides the Fe XVIII and Fe X, there are still many unknown low-temperature emission lines in the ARs of 94 Å (Del Zanna 2013). The Fe XIV, one of the new emission lines, the count rate is much greater than Fe X. In this paper, our target is to find a better method to fit the low-temperature components of the 94 Å.

2. Nonlinear Regression for Outlier Detection

Usually, the solar corona is dominated by the quiet Sun. The number of ARs is a small amount, which can be considered as an outlier object compared to the whole solar corona. In machine learning, anomalous objects are called outliers (Ghosh & Vogt 2012). An outlier is an object that significantly deviates from the rest of the data points, is not subject to the same statistical model as the rest of the data set, and arises from a completely different mechanism. So the detection of these anomalous data points is outlier detection. The different regions in the solar corona have completely different physical mechanisms. The high-temperature regions can be seen that the data points generated by a completely different statistical model in a coronal image.

Among the six Fe channels, many same emission lines exist between different channels, while different channels have their unique emission lines. Del Zanna (2013) tried to find the high-temperature outlier component of 94 Å by replacing the common low-temperature feature of 94 Å with a linear method and did achieve some results. However, the connection between AIA is so complex that a simple linear method has many limitations. Therefore, a nonlinear method is needed to accomplish this.

Table 1
Predicted Count Rates of 94 Å

No	Line	Wavelength (Å)	Temperature (MK)	CH	QS	AR	FL
	Mg VIII	94.07	5.9	0.03	⋯	⋯	⋯
	Fe XX	93.78	7.0	⋯	⋯	⋯	0.10
	Fe XVIII	93.93	6.85	⋯	⋯	0.74	0.85
94 Å	Fe X	94.01	6.05	0.63	0.72	0.05	⋯
	Fe VIII	93.47	5.6	0.04	⋯	⋯	⋯
	Fe VIII	93.62	5.6	0.53	⋯	⋯	⋯
	Cont.			0.11	0.12	0.17	⋯

Note. The count rates of 94 Å. Coronal hole (CH), quiet Sun (QS), active region (AR) and flare (FL) plasma, and temperature is log of the temperature of maximum abundance.

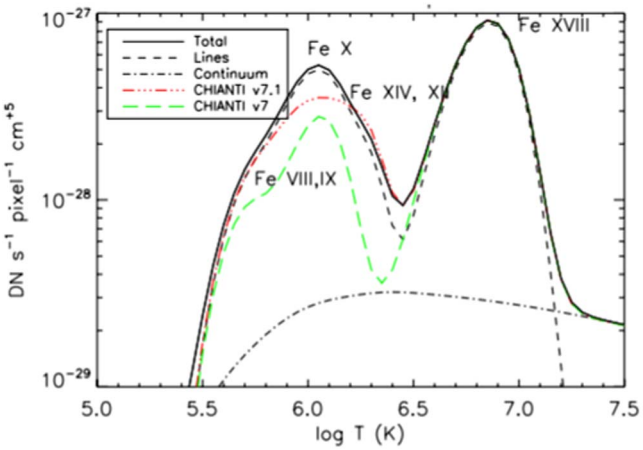

Figure 2. AIA 94 Å Responses (Del Zanna 2013).

There is a great advantage of machine learning in employing nonlinear classification and regression. For the complex nonlinear relationship between AIA channels, machine learning is used to extract the common information of different AIA channels, such as the common low-temperature component that exists in the 94 Å and other low-temperature channels. Then the common component is compared with the original 94 Å to obtain the outlier component which is not included in the relationship, or the high-temperature component in 94 Å.

3. Data Set and Data Processing

The high-temperature regions tend to be concentrated in the core of ARs, so in this paper, we select ARs in the solar corona as our data set. For convenience, we choose the ARs as close to the center of the solar corona as possible. All the AIA data in this paper are Level 1 data of 12 s EUV which are downloaded from JSOC. Then the spike data are removed and uniformly preprocessed as Level 2 data. For subsequent training, all ARs are uniformly cropped to $400'' \times 800''$.

Considering the solar rotation and projection of the image, there is a certain gap between the images of different channels of AIA because of the shooting time and exposure time, in order to eliminate the error, it is necessary to align the images of different channels. Here we use the program *aia_prep* of solar physics software (SSW) to calibrate the consecutive Level1 AIA images and generate the standard AIA images by setting the center of the solar as the reference data. In the cropping of the active area, SSW's *get_sub_map* and *drot_map* are used to eliminate spin and align the images based on a set time for subsequent DEM calculations.

On the selection of the training set and validation set, to obtain a sufficient number of types of ARs, suitable ARs data are selected with a time interval of one day starting from 2021 December 15, 13:30 UTC to 2022 February 30, 13:30 UTC. Then divided into 160 sets of the training sets and 10 sets of the validation sets.

On the selection of the test set, considering the existence of different ARs, we choose ARs date of NOAA in Table 2 as the test set to examine the training effect and the result. In the result presentation, we further crop the images to show the core of the ARs as well as its some surrounding parts.

There are some difficulties in the original data for measuring the temperature of AIA. For convenience, all the data need to be processed. Then we calculate the DEM by the method proposed by Cheung et al. (2015) for temperature analysis in the later paper. A set of six Fe channels of AIA was used for DEM calculating and the temperature coverage was set to 4.0–9.0 MK with an interval of 0.5 MK. Finally, we regenerate the AIA data based on the results of DEM and response functions of AIA for later training and result testing.

4. Method

The emergence of deep learning and neural networks has shown great advantages in handling complex nonlinear regression. In 2016, to solve the degradation problem of the neural network, He et al. (2016) proposed the residual network. He added an identify mapping based on the forward neural network. With its obvious advantages in large deep networks,

Table 2
A Survey of Solar Active Regions

No.	NOAA	Date	X_{cen}	Y_{cen}	Filename
1	11089	2010 Jul 23 15:03:08	−348.5	−442	AIA20100723_150308_0094.fits
2	11109	2010 Sep 29 23:51:38	335	250	AIA20100929_235138_0094.fits
3	11147	2011 Jan 21 14:10:50	−57	453.5	AIA20110121_141050_0094.fits
4	11150	2011 Jan 31 11:25:02	−508	−272.5	AIA20110131_112502_0094.fits
5	11339	2021 Nov 10 11:33:14	406	206.5	AIA20111110_113314_0094.fits

Note. X_{cen} and Y_{cen} are the NOAA active region coordinates differentially rotated to the mid-point of the EIS raster.

in this paper, we choose to build the neural network based on the residual network.

According to Table 3 (O'dwyer et al. 2010), it can be found that the 131 Å is a high-temperature emission line, and Fe XIV (6.45 MK) produces the main count rates of the 335 Å, neither of which is suitable for the replacement of low-temperature component of the 94 Å. The 171, 193, 211 Å can be fond that their all radiation temperature in the ARs is below 6.45 MK, which is the main part of the low temperature components of the 94 Å. Based on this, the 171, 193, 211 Å are chosen as the channels to fit the low-temperature component of the 94 Å in this paper. For the composition of data set, the 171, 193, and 211 Å are used as the input set, and the 94 Å is the label set, the network structure is a three-to-one network. The prediction of the low-temperature component of 94 Å is achieved by the 171, 193, 211 Å, and then the prediction comparing with the original 94 Å to get the high-temperature component of 94 Å, or Fe XVIII.

The network model is a generative model based on the residual network, and the convolutional kernel is designed with 3×3. The network contains a total of 10 layers. The input data of the network is a $3 \times 667 \times 1334$ image matrix, which is first up-dimensioned by the convolutional layer and the batch normalization layer to get a $64 \times 667 \times 1334$ image matrix, and then enters the residual network, and the final output gets a $1 \times 667 \times 1334$ prediction image (see Figure 3).

The outlier detection algorithm is used in this paper, our target is to detect the high-temperature region of the ARs. So it is necessary to improve the fitting accuracy of the low-temperature component part of the quiet regions as much as possible. However, considering the low SNR of the quiet regions of 94 Å, the noise interference in the quiet region is more serious, and using the quiet regions directly as the label for training will amplify the noise. So we choose to add a mask to removing the hot core of ARs in our training process. However, the ARs are usually irregular, and there are great difficulties in uniform masking, therefore, we propose the following algorithm:

The training target of our neural network is the quiet regions of 94 Å. For the overall image, the loss of fitting the r hot ARs will be obviously larger than the loss of the quiet region. In the design of the loss function, we calculate the loss of each pixel of the predicted image in each training epoch and find the standard deviation of the all loss. With reference to the 3σ principle, only the loss which is less than a certain standard will be retained, then we calculate the mean of remaining loss and enter the next epoch of training. Meanwhile the loss greater than the certain standard is rounded off and stored as the mask, (can be seen in Figure 4). After several rounds of experimental testing, we choose $1.5 \times \sigma$ as the threshold value, which can remove the hot core well. After the model is trained and stabilized, the influence of the hot core of ARs on the neural network can be well removed and can be directly applied to the whole ARs in the test set.

Table 3
The Predicted Count Rates of ARs in Different AIA

No	Line	Wavelength (Å)	Temperature MK	AR
94 Å	Fe XVIII	93.93	6.85	0.74
	Fe X	94.01	6.05	0.05
	Cont.			0.17
131 Å	Fe VIII	130.94	5.6	0.09
	Fe VIII	131.24	5.6	0.13
	Cont.			0.54
171 Å	Ni XIV	171.37	6.35	0.04
	Fe IX	171.07	5.85	0.80
193 Å	Ca xiv	193.87	6.55	0.04
	Fe XII	195.12	6.2	0.17
	Fe XII	193.51	6.2	0.17
	Fe XII	192.39	6.2	0.08
	Fe XI	188.23	6.15	0.04
	Cont.			0.05
211 Å	Fe XIV	211.32	6.3	0.39
	Fe XIII	203.83	6.25	0.07
	Fe XIII	209.62	6.25	0.07
	Cont.			0.07
335 Å	Fe XVI	335.41	6.45	0.86
	Fe XIV	203.83	6.3	0.04

Note. The count rates of ARs. The active region (AR) and temperature is log of the temperature of maximum abundance.

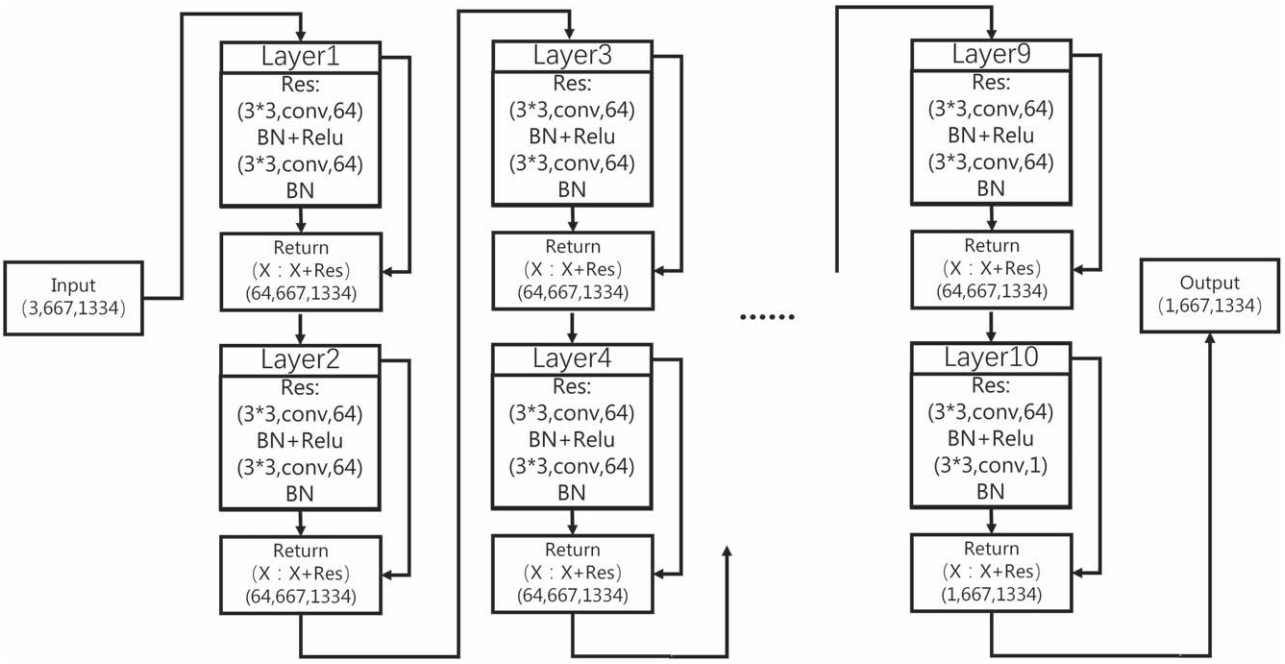

Figure 3. Overall architecture of the ResNet Model.

The activation function for each convolutional layer is chosen as Rectified Linear Activation Function (ReLU function) (Nair & Hinton 2010)

$$f(x) = \max(0, x). \tag{5}$$

Here max is the maximum function and x is the input of the previous layer. With the ReLU function, a nonlinear factor is added to the network, making it easier to extract more complex information.

The model uses the SGD optimizer (Bottou 2012)

$$\boldsymbol{W} \leftarrow \boldsymbol{W} - \eta \frac{\partial L}{\partial \boldsymbol{W}}. \tag{6}$$

Here W is the weight parameter, the gradient of the loss function about W is $\frac{\partial L}{\partial \boldsymbol{W}}$, and η is the learning rate, which is taken as 0.0001 in this paper. SGD is a commonly used optimization algorithm that possesses adaptive and stable results.

To verify the results of neural networks and linear fitting, the following three methods are chosen as the evaluation metrics (Sara et al. 2019).

Structural Similarity (SSIM) is a metric used to measure the similarity of images:

$$\mathrm{SSIM}(x, y) = \frac{(2\mu_x\mu_y + C_1)(2\sigma_{xy} + C_2)}{(\mu_x^2 + \mu_y^2 + C_1)(\sigma_x^2 + \sigma_y^2 + C_2)} \tag{7}$$

where $C1$, $C2$, $C3$ are constants, μx, μy are the mean value of the image x, y, and σx, σy are the standard deviation of image x, y.

Mean Square Error (MSE) is used to measure how well the predicted value $\hat{Y}_i$ matches the true value:

$$\mathrm{MSE} = \frac{1}{n}\sum_{i=1}^{n}(Y_i - \hat{Y}_i)^2 \tag{8}$$

where $\hat{Y}_i$ is the prediction of Y.

Peak Signal to Noise Ratio (PSNR) is a metric used to evaluate the quality of processed images

$$\mathrm{PSNR} = 10 \cdot \log_{10}\left(\frac{\mathrm{MAX}_I^2}{\mathrm{MSE}}\right) \tag{9}$$

where MAX_I^2 is the max pixel value of image I.

Taking into account the special nature of AIA images, log processing was applied to the images in the subsequent image display to enhance the contrast. At the same time, since the obtained Fe XVIII is an outlier component, there is a certain negative value. In order to eliminate this part of the influence, an intensity threshold of 10 was set for the obtained outlier component to eliminate the negative value influence of 94 Å. In the residual contrast, in order to eliminate the influence of negative values, an intensity threshold of 2 was set.

Figure 4 shows the training process and can be seen that the network converges quickly, with a stable loss after 50 epochs. The average loss of the training set decreases smoothly and finally stabilizes below 1. The average loss of the valid set also quickly converged and stabilized after a large shakeout. It also can be seen that the ARs in the three images of the input set are not obvious, and therefore the AR cores are not obvious in the predicted images. However, the AR core in 94 Å is very

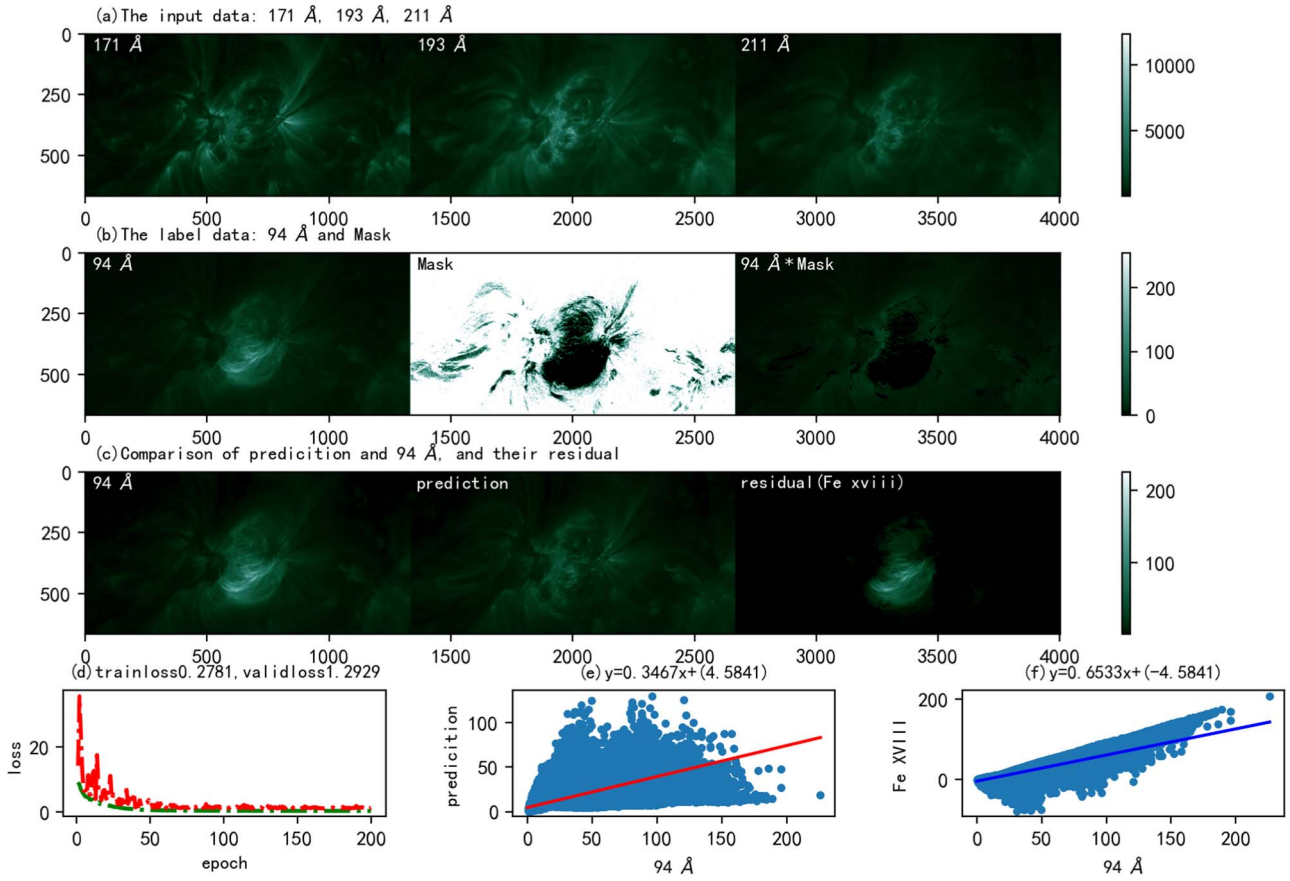

Figure 4. The training process. (a) The input data; (b) is the 94 Å and the mask (c) is the comparison, the residual (Fe XVIII) is the 94 Å minus the prediction; (d) is the loss; (e) is the comparison of prediction and 94 Å; (f) is the comparison of residual (Fe XVIII) and 94 Å.

prominent, and the high temperature region is very obvious in the outlier component of 94 Å compared with the prediction images. In the intensity comparison, the intensity of the predicted results compared to 94 Å is significantly weaker than the intensity of the outlier component. The high-temperature component accounts for a larger proportion in the 94 Å.

5. Results

To verify the effectiveness of the neural network, we use some classical ARs as the test set to verify the relationship of AIA, and also obtain the outlier high-temperature components, and analyze the similarities and differences between the results of the DEM and Del's method.

5.1. The Correlation Analysis of AIA

From the results in Table 4, it can be seen that both Del's linear fitting and the neural network can make a good-quality image fitting. The SSIM of two methods can almost reach up to 85% or higher. All the PSNR of the prediction images are not less than 25, indicating a good-quality image prediction. But the MSE of images is very high, which means the values of prediction images and original images have great distinctions. In Figure 5, it can be clearly seen in AR 11339 that in the core of the ARs, both predicted images miss many structures. The SSIM of both results is close to 90% and the PSNR of the images is below 30, but the MSE values are up to 100. This indicates that the quality of the predicted images is not very good and many components are still not fitted. Meanwhile, compared to Del's method, the prediction results obtained by the neural network are lower in SSIM only 87%, but both PSNR and MSE are better, while in the intensity comparison, the intensity of the prediction results of the neural network is higher than that of Del by about 40%, indicating that the prediction results of the neural network have significantly more low-temperature components and the intensity is closer to that of the original 94 Å image than Del's results.

Compared with the original 94 Å, the prediction images both have a high similarity. But in the comparison between Del's method and the neural network, we can see that the value of SSIM and PSNR are close to each other. But the MSE of the neural network is significantly smaller than Del's method, and

Table 4
The Statistical Results of Comparison of Prediction Image between the Del's Method and Neural Network

No.	NOAA	SSIM (A/B)	MSE (A/B)	PSNR (A/B)	Comparison (B/A)
1	11089	0.9545/0.9560	17.9115/11.4112	36.7086/38.6666	1.4086
2	11109	0.8540/0.8887	11.8151/8.2368	29.7831/31.3499	1.2907
3	11147	0.9817/0.9903	36.0018/29.3719	39.4107/40.2946	1.4156
4	11150	0.9554/0.9488	16.8259/11.6828	34.5993/36.1836	1.3366
5	11339	0.9067/0.8748	127.3522/96.7364	25.9940/27.1881	1.3850

Note. A is the result of Del's method, and B is the result of neural network. The comparison is the neural network divided by Del's method.

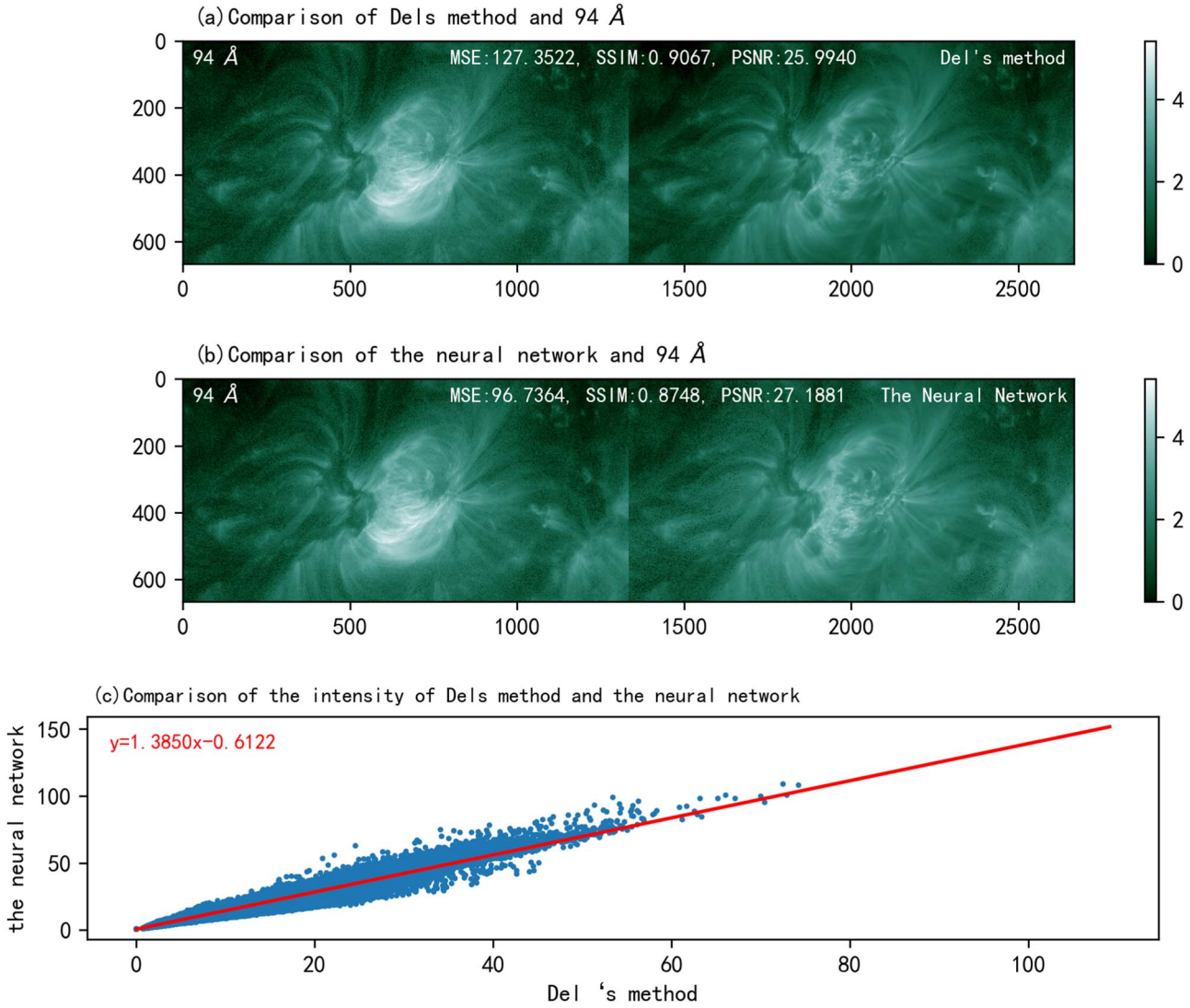

Figure 5. The comparison of original 94 Å and the prediction images by Del's method and the neural network.

Table 5
The Results of Comparison between the Del's Method and Neural Network

No.	NOAA	SSIM (A/B)	MSE (A/B)	PSNR (A/B)
1	11089	0.9684/0.8958	16.9990/69.4549	34.0291/27.9163
2	11109	0.9640/0.8924	4.2295/16.9924	31.3789/25.3392
3	11147	0.9856/0.9524	14.4278/61.3715	43.0166/36.7289
4	11150	0.9864/0.9463	5.3387/27.2908	37.0107/29.9250
5	11339	0.9711/0.9090	25.8862/91.0982	32.6571/27.1927

Note. A is the result of Del's method, and B is the result of neural network.

the intensity of Del's method is only about two-thirds of the neural network. It means that the low-temperature component of the neural network is fitted with more content and higher intensity, which is closer to the original image excluding the high-temperature regions.

The 94 Å consists of multiple emission lines, to extract the common low-temperature emission lines, we used the 171, 193, and 211 Å to fit the 94 Å. From the above results, it can be found that both methods extract the common contents from the 94 Å by the combination of some other AIA channels.

5.2. The Extraction and Analysis of High-temperature Regions

According to the response functions of 94 Å, the temperature range of the high-temperature is set to 6.45–7.0 MK to compare with the high-temperature outlier components obtained from Del's method and the neural network. In order to compare the difference between the results of the two methods, we subtracted the high-temperature of Del's method from the neural network, and the temperature range of the low-temperature was set to 6.1–6.45 MK to compare.

From the results in Table 5, it can be seen that both methods achieve a good-quality image similarity. The SSIM of the two methods can reach more than 89% and the PSNR can also reach more than 27, but the MSE still has disparity. The SSIM of Del's method is above 96%, and the PSNR is above 30, which are all higher than the neural network. On the comparison of the MSE, the neural network is higher than Del's method. From the actual image comparison (see Figure 6), most of the structures can be well-fitted, and some details are missing. Especially in the neural network, it can be seen in AR 11339 that a large number of low bright areas are lost and there is a large difference with the high-temperature results calculated by the DEM. In AR 11339, both the SSIM of two methods is high, but compared with Del's method, the SSIM, PSNR, MSE of the neural network all are worse, indicating that the high-temperature components obtained by the neural network are significantly less than Del's method and DEM.

To compare the difference between Del's method and the neural network, we subtract the result of the neural network from the results of the Del's method and the 6.45–7.0 MK calculated by the DEM. We compare the residuals with the low-temperature component (6.1–6.45 MK) of the 94 Å. The results in Table 6 show that the SSIM almost can reach more than 60%, the PSNR is above 20, which means the image similarity is high. Especially in AR 11109, its SSIM of two results are over 49%, and the PSNR are around 20. Figure 6 also shows that inner structures are similar, but the residual has more details than the low-temperature component. The MSE of both the residuals are not very high, indicating the intensity difference between the residual and the low-temperature component is not large. But the MSE of residual of the DEM is larger than Del's method, meanwhile the residual has more details. The residuals made by the DEM and Del's method have a great similarity with the low-temperature component of 6.1–6.45 MK. But the high-temperature obtained by the DEM is more than the results obtained by Del's method and the neural network.

According to the previous section, the Fe XVIII is the main high-temperature emission line in the ARs of the 94 Å, and its typical temperature is 6.85 MK with a peak temperature is 7.0 MK, so the high temperature of 6.45–7.0 MK calculated by the DEM can be considered as the Fe XVIII. From the above results, it can be found that both methods can obtain Fe XVIII well, but the results of the neural network miss more content. Meanwhile, the Fe XIV, a new emission line found in the ARs of the 94 Å, a typical temperature is 6.3 MK. So we consider the low temperature of 6.1–6.45 MK as the Fe XIV and we find that there is a large similarity between the residuals of Del's method and neural networks and the Fe XIV.

Both Del's methods and the neural network can achieve a good quality of extracting the Fe XVIII from the 94 Å. We also find that compared with Del's algorithm, the neural network removed more Fe XIV components, and obtained more pure Fe XVIII components than the results of DEM and Del's method.

5.3. Summary

There are complex relationships between AIA multi-channels. Based on Del's method, we used three channels the 171, 193, 211 Å to achieve the prediction of the 94 Å. The results of the neural network are close to the Del's method and DEM, but the values of low-temperature regions are higher.

The high-temperature range of 6.45–7.0 MK of the 94 Å includes not only Fe XVIII. The high temperature components obtained by both the Del algorithm and the neural network are very close to the Fe XVIII calculated by the DEM, but Del's method and the results of DEM has significantly more Fe XIV compared to the neural network. The neural network algorithm obtains the Fe XVIII component with fewer low-temperature

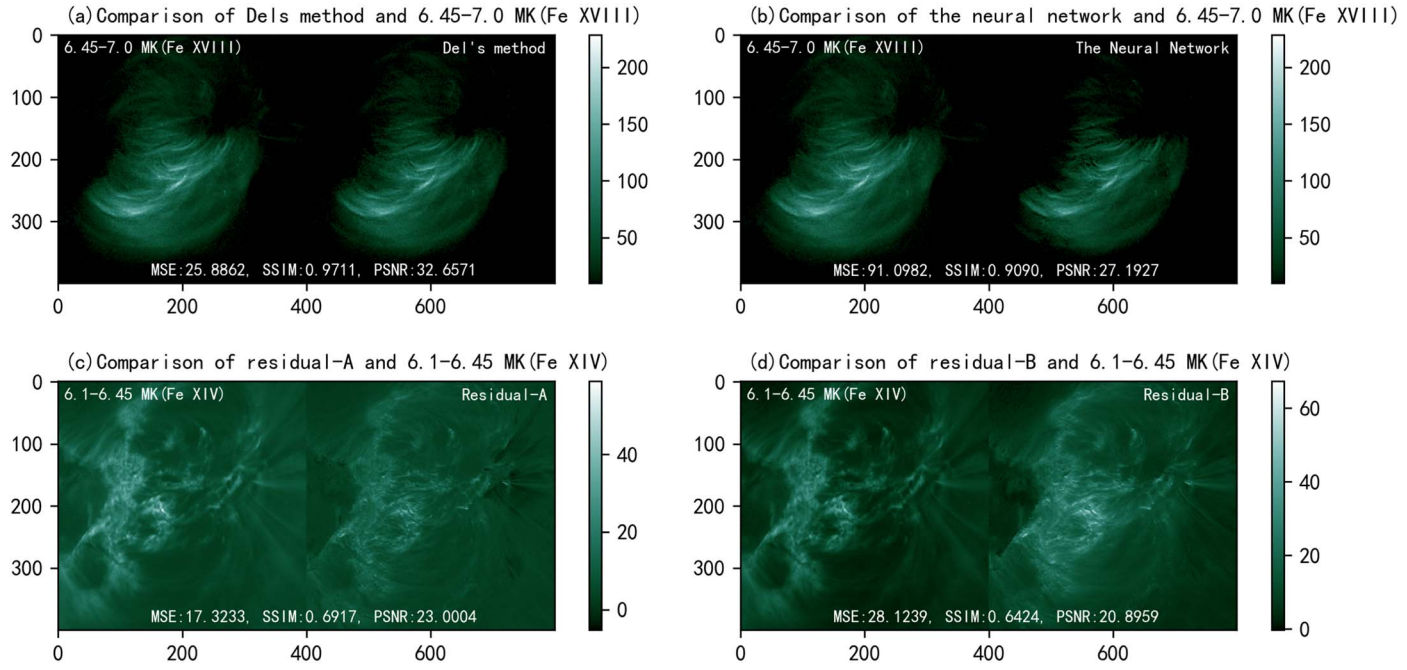

Figure 6. The residual-A is the residual that the Fe XVIII by Del's method minus the Fe XVIII by the neural network. The residual-B is the residual that the Fe XVIII by the DEM minus the Fe XVIII by the neural network.

Table 6
The Results of Comparison between the Residual-A and Residual-B

No.	NOAA	SSIM (A/B)	MSE (A/B)	PSNR (A/B)
1	11089	0.6986/0.6423	13.2092/25.9691	23.5651/20.6293
2	11109	0.5609/0.4964	29.8847/17.3333	19.2621/21.6278
3	11147	0.6216/0.6460	24.3258/35.2457	24.8352/23.2248
4	11150	0.6227/0.5775	14.9405/11.1108	22.2641/23.5503
5	11339	0.6917/0.6424	17.3233/28.1239	23.0004/20.8959

Note. A is the results of residual-A, and B is the results of residual-B.

components, but still retains some non-high-temperature emission lines.

6. Discussion and Future Work

In this paper, we tried to extract the high-temperature regions using a new approach with neural networks and did get different results. The brand-new results produced large differences from the results of DEM and Del's method. But there are still some factors that should be considered.

1. The physical mechanisms that make up the solar corona are very complex. The DEM algorithm also has a large uncertainty, and the high-temperature results contain not only Fe XVIII, but also many unknown emission lines.

2. The amount of experimental data is limited. The amount of experimental data in this paper is small, and the image quality of the training set is unstable, the amount of data will be expanded in later work and the training set with more obvious active areas will be selected in the image screening.

Acknowledgments

The data used here are courtesy of the SDO science teams. In particular, we appreciate downloading data conveniently from JSOC. This work was supported by the National Natural Science Foundation of China under Grant Nos. U2031140, 11873027, and 12073077.

ORCID iDs

Li-Yan Sun https://orcid.org/0000-0002-2113-7888
Kai-Fan Ji https://orcid.org/0000-0001-8950-3875
Hui Liu https://orcid.org/0000-0003-2714-6811

References

Acton, L., Bruner, M., Lemen, J., et al. 1992, Sci, 258, 618
Bottou, L. 2012, Neural Networks: Tricks of the Trade (2nd ed.; Berlin: Springer), 421
Cheung, M. C., Boerner, P., Schrijver, C., et al. 2015, ApJ, 807, 143
Del Zanna, G. 2013, A&A, 558, A73
Domingo, V., Fleck, B., & Poland, A. I. 1995, SoPh, 162, 1
Ghosh, D., & Vogt, A. 2012, in 2012 Joint Statistical Meetings Program Committee, 3455
Golub, L., Bookbinder, J., DeLuca, E., et al. 1999, PhPl, 6, 2205
He, K., Zhang, X., Ren, S., & Sun, J. 2016, in Proc. IEEE Conf. on Computer Vision and Pattern Recognition, 770
Hundhausen, A. 1993, JGRA, 98, 13177
Landi, E., Del Zanna, G., Young, P., Dere, K., & Mason, H. 2011, ApJ, 744, 99

Lemen, J. R., Title, A. M., Akin, D. J., et al. 2012, SoPh, 275, 17
Mulay, S. M., Matthews, S., Hasegawa, T., et al. 2018, SoPh, 293, 1
Nair, V., & Hinton, G. E. 2010, in Proc. 27th Int. Conf. on Machine Learning (ICML-10), 807
O'dwyer, B., Del Zanna, G., Mason, H., Weber, M., & Tripathi, D. 2010, A&A, 521, A21
Orrall, F. Q. 1981
Pesnell, W. D., Thompson, B. J., & Chamberlin, P. 2012, The Solar Dynamics Observatory (SDO) (Berlin: Springer)
Sara, U., Akter, M., & Uddin, M. S. 2019, Journal of Computer and Communications, 7, 8
Tsuneta, S., Ichimoto, K., Katsukawa, Y., et al. 2008, SoPh, 249, 167
Warren, H. P., Winebarger, A. R., & Brooks, D. H. 2012, ApJ, 759 141